A&A 523, A29 (2010)
DOI: 10.1051/0004-6361/200913839

Astronomy & Astrophysics

Wide field CO $J = 3 \rightarrow 2$ mapping of the Serpens cloud core

O. Dionatos[1,2], B. Nisini[2], C. Codella[3], and T. Giannini[2]

[1] Centre for Star and Planet Formation, Natural History Museum of Denmark, University of Copenhagen, Øster Voldgade 5-7, 1350 Copenhagen, Denmark
e-mail: odysseas@snm.ku.dk
[2] INAF, Osservatorio Astronomico di Roma, via di Frascati, 33 00040 Monte Porzio Catone (RM), Italy
[3] INAF, Osservatorio Astrofisico di Arcetri, Largo E. Fermi 5, 50125 Firenze, Italy

Received 9 December 2009 / Accepted 28 July 2010

ABSTRACT

Context. Outflows provide indirect means to gain insight into diverse star formation-associated phenomena. At the level of individual protostellar cores, both outflows and the intrinsic core properties can be used to study the mass accretion/ejection process of heavily embedded protostellar sources.
Aims. The main objective of the paper is to study the overall outflow distribution and its association with the young population of the Serpens Core cluster. In addition, the paper addresses the correlation of the outflow momentum flux with the bolometric luminosity of their driving sources using this homogeneous dataset for a single star-forming site.
Methods. An area comprising $460'' \times 230''$ of the Serpens cloud core was mapped in ^{12}CO $J = 3 \rightarrow 2$ with the HARP-B heterodyne array at the James Clerk Maxwell Telescope; $J = 3 \rightarrow 2$ observations are more sensitive tracers of hot outflow gas than lower J CO transitions; combined with the high sensitivity of the HARP-B receptors outflows are sharply outlined, enabling their association with individual protostellar cores.
Results. Most of ~20 observed outflows are found to be associated with known protostellar sources in bipolar or unipolar configurations. All but two outflow/core pairs in our sample tend to have a projected orientation spanning roughly NW-SE. The overall momentum driven by outflows in Serpens lies between 3.2 and 5.1×10^{-1} $M_{\odot}\,\mathrm{km\,s^{-1}}$, the kinetic energy from 4.3 to 6.7×10^{43} erg, and momentum flux is between 2.8 and 4.4×10^{-4} $M_{\odot}\,\mathrm{km\,s^{-1}\,yr^{-1}}$. Bolometric luminosities of protostellar cores based on Spitzer photometry are found up to an order of magnitude lower than previous estimations derived with IRAS/ISO data.
Conclusions. We confirm the validity of the existing correlations between the momentum flux and bolometric luminosity of Class I sources for the homogenous sample of Serpens, though we suggest that they should be revised by a shift to lower luminosities. All protostars classified as Class 0 sources stand well above the known Class I correlations, indicating a decline in momentum flux between the two classes.

Key words. stars: formation – ISM: jets and outflows – ISM: molecules – submillimeter: ISM

1. Introduction

The Serpens cloud core is an active region of low-mass star formation harboring a great diversity of star-birth associated phenomena. Since its first identification as a stellar nursery by Strom et al. (1976), studies have revealed several millimeter sources identified as protostellar condensations (Testi & Sargent 1998), ~10 Class 0 candidates (Casali et al. 1993; Hurt & Barsony 1996; Harvey et al. 2007; Winston et al. 2007), at least 20 Class I sources (Kaas et al. 2004; Winston et al. 2007; Harvey et al. 2007), along with a more evolved population of ~150 Class II sources detectable in the near-IR (Eiroa & Casali 1992; Giovannetti et al. 1998; Kaas 1999). The remarkably high stellar density and star formation efficiency (~5% Evans et al. 2003), along with its proximity (~310 pc, de Lara et al. 1991), have rendered Serpens an observationally attractive site for star formation studies, as shown by the extensive literature.

Star formation activity in Serpens is also manifested by dynamic mass-loss phenomena, such as optical and near-IR detections of Herbig Haro objects (Gomez de Castro et al. 1988; Reipurth & Eiroa 1992; Davis et al. 1999; Ziener & Eislöffel 1999), near-IR molecular jets (Hodapp 1999; Eiroa et al. 1997; Herbst et al. 1997), and molecular outflows. Individual outflows in Serpens have been recorded in a wide variety of molecular tracers and different transitions; e.g. CS in Testi et al. (2000), Mangum et al. (1996), Wolf-Chase et al. (1998); H_2CO in Mangum et al. (1996); CH_3OH in Garay et al. (2002) and Testi et al. (2000); HCO^+ in Gregersen et al. (1997) and Hogerheijde et al. (1999); HCN, SO, and SiO in Hogerheijde et al. (1999) and Garay et al. (2002); NH_3 in Torrelles et al. (1992). Wide-field, homogenous outflow mapping of the Serpens Core has so far only been performed at the $J = 1 \rightarrow 0$ (Narayanan et al. 2002) and $J = 2 \rightarrow 1$ (White et al. 1995; Davis et al. 1999) transitions of carbon monoxide. This region has also been mapped very recently in the CO $J = 3 \rightarrow 2$ as part of the JCMT Gould Belt Legacy Survey (GBS) to investigate the large-scale mass and energetics of the cloud (Graves et al. 2010).

In this paper, we present a new CO $J = 3 \rightarrow 2$ map covering $460'' \times 230''$ of the Serpens core, with the aim of studying the individual outflows of the region in unprecedented detail. Compared to lower J maps, the higher energy transition (corresponding to a smaller beam for the same dish aperture) coupled with the higher sensitivity reached by the HARP-B observations delineate individual outflows better than before. The advantage of higher energy transitions in mapping outflows is illustrated in Fig. 3 of Narayanan et al. (2002), where higher-J CO close-ups are presented towards the Class 0 source SMM4: higher J maps suffer from much less confusion because the "warm" outflowing

gas is disentangled better from the "cold" cloud material. This is particularly important in Serpens, where protostellar sources are closely clustered and their outflows tend to overlap and mix.

Distinguishing individual outflows enables detailed investigation of a series of phenomena related to their generation. Outflow emission traces the swept-up ambient gas that has been entrained by a jet/wind that is directly linked to a protostar; in the opposite sense, i.e. backtracking the outflow lobes, outflows can be associated with individual protostellar sources. In addition, outflow activity is thought to begin almost simultaneously with the formation of a hydrostatic core, so that outflows paired to protostellar clumps can be employed as independent means to identifying embedded protostars (e.g. Hatchell & Dunham 2009).

Alternatively, outflows can be employed to study the accretion and mass ejection process in otherwise highly obscured and inaccessible protostellar environments. There is increasing evidence that the momentum flux or "thrust" of molecular outflows is linked to the luminosity of the protostellar core (e.g. Cabrit & Bertout 1992; Bontemps et al. 1996; Wu et al. 2004; Hatchell et al. 2007a). Such a correlation implies that, independently of the details of the mass accretion and ejection mechanisms, both quantities are energetically governed in common by infall. Still, observational determination of both outflow thrust and bolometric luminosity in clustered protostellar environments remains challenging, so their exact correlation is poorly defined.

In this context, in Sect. 2 we present the HARP-B observations and give an outline of the data reduction. Morphological characteristics of outflows and their association with individual protostellar sources are discussed in Sect. 3. In Sect. 4, we derive outflow properties such as the column density, mass, momentum, kinetic energy and the momentum flux. In Sect. 4.4 we estimate the bolometric luminosity by employing recent Spitzer mid and far-IR photometry for the sources associated with the observed outflows. Section 5 examines the correlation between the bolometric luminosity and momentrum flux for the homogenous sample of sources in Serpens. In the same section, the relation between the bolometric luminosity with the outflow mass and mechanical luminosity are discussed. Finally, in Sect. 6 we summarize and draw the main conclusions of this work.

2. Observations and data reduction

The ^{12}CO $J = 3 \rightarrow 2$ on-the-fly (OTF) maps were obtained between 9 April and 9 June 2007 with the HARP-B heterodyne array (Smith et al. 2008) and ACSIS correlator (Dent et al. 2000; Lightfoot et al. 2000) on the James Clerk Maxwell Telescope (JCMT). The mapped area was covered by consecutive scans in "basket-weave" mode at a position angle of 322°. Each scan was offset from its surroundings by 87.3″ in the orthogonal direction, and the signal was integrated every 7.3″ along the scan direction with an effective integration time of 3 seconds per point. The resulting map dimensions are $7.7' \times 4.3'$, but the fully sampled area is somewhat smaller as the borders are not fully sampled because a number of HARP-B receptors were non-functional at the time of the observations. The spectral resolution is 488 KHz which corresponds to 0.41 km s^{-1} at the frequency of 345.795 GHz. Single maps were co-added and initial data cubes converted with the makecube command in the STARLINK/SMURF package. The resulting map is centered on $\alpha = 18^{\rm h}29^{\rm m}49\overset{\rm s}{.}7$, $\delta = 01°15'22\overset{''}{.}8$ (epoch J2000) and has a pixel size of 7.3″, which is just below the Nyquist sampling limit for the ∼14″ beamwidth of each HARP-B receptor. A correction of $n_{\rm MB} = 0.6$ for the main beam efficiency was applied, and further reduction was performed with the CLASS/GreG packages. The mean rms noise in brightness temperature $T_{\rm B}$ per spectrum across the map is 0.08 K, which is slightly deeper than the 0.1 K reported in Graves et al. (2010), while the 1-sigma rms level for the map is at 0.27 K km s^{-1}. Pixels exhibiting an rms noise greater than 6-sigma of the mean were discarded in the final maps.

3. Outflow morphology

3.1. Overall

The overall morphology of the high-velocity gas in the investigated region, can be seen in Fig. 1, presenting the CO $J = 3 \rightarrow 2$ intensity map integrated over the high velocity blue-shifted (-30 km s^{-1} $\leqslant V_{\rm LSR} \leqslant 0$ km s^{-1}) and red-shifted (18 km s^{-1} $\leqslant V_{\rm LSR} \leqslant$ 48 km s^{-1}) wings, superimposed on a (grayscale) Spitzer-MIPS 24 μm image. The 24 μm band was selected because it is sensitive in tracing continuum emission from protostellar envelopes surrounding deeply embedded sources, and providing more superior spatial resolution than the other, longer wavelength MIPS bands. Figure 1, delineates the extent of the mapped area and indicates areas that are discussed in detail in Sect. 3.2–3.4. CO $J = 3 \rightarrow 2$ representative spectra sampling the map of Fig. 1 at different offsets are displayed in Fig. 2; dashed lines mark the velocity intervals over which the intensity is integrated, and the solid line indicates the cloud's systemic velocity (∼9 km s^{-1}), coinciding with the self-absorption profile. Low-velocity cuts at ±9 km s^{-1} from the body of the line ensure that the ambient contribution is excluded. High-velocity cuts are imposed by the rms noise level of the maps; the higher sensitivity obtained with these observations (∼4 times higher than the one reached by Davis et al. 1999, with the same telescope) allow the high velocity cutoffs to be extended to ∼±40 km s^{-1} from the $V_{\rm LSR}$.

In Fig. 2, two types of high-velocity wing morphologies are distinguishable. In the lower two panels, high-velocity gas forms continuous, fading-off wings as a function of velocity from $V_{\rm LSR}$; in the upper two panels high-velocity gas exhibits a semi-detached distribution, with a secondary peak tracing clumps of high-velocity blue- and red-shifted gas. The latter wing morphology is indicative of high-velocity "bullets" of gas, commonly observed in molecular jets from Class 0 protostars (e.g. Bachiller et al. 1991)

The large-scale spatial distribution of the poorly evolved Class0/I young stellar objects in Serpens, which is identified by their SED (Hurt & Barsony 1996; Larsson et al. 2000; Winston et al. 2007), infrared excess, and spectral indices (Kaas 1999; Kaas et al. 2004; Enoch et al. 2009; Winston et al. 2007), or detection of luminous millimeter and submillimeter continuum sources (Casali et al. 1993; Testi & Sargent 1998; Davis et al. 1999; Williams & Myers 2000) display concentrations into two clumps located at the northwest (areas A and B) and southeast (area C), separated by ∼200″ (Casali et al. 1993), as traced by the 24 μm MIPS background image in Fig. 1. Not surprisingly, most of the outflow activity observed in same figure is tightly constrained to the same northwest and southeast clumps, because powerful molecular outflows are known to be driven by very young stellar objects (Richer et al. 2000). Twelve out of fourteen sources classified as bona-fide Class0/I objects (Winston et al. 2007) lie within the extent of the CO $J = 3 \rightarrow 2$ HARP-B map.

The distribution of more evolved Class II sources, in contrast, shows no signs of clustering but is found to be more

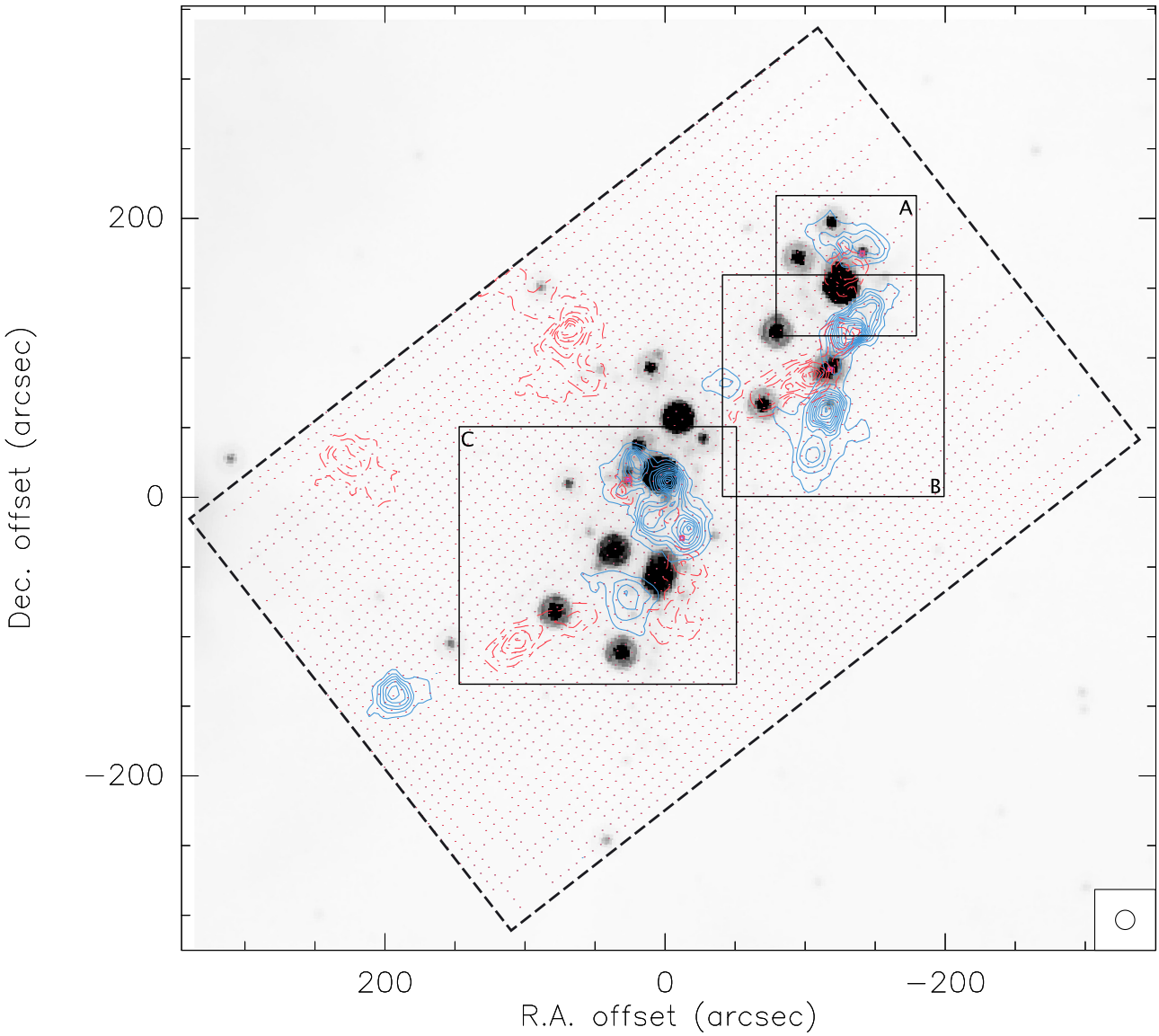

Fig. 1. High-velocity CO $J = 3 \rightarrow 2$ outflow map superimpsed on an MIPS band 1 (centered on 24 μm) image of the Serpens cloud core. Solid (blue) contours delineate blue-shifted gas (integrated over -30 km s^{-1} $\leqslant V_{\rm LSR} \leqslant 0$ km s^{-1}, while dashed (red) contours delineate red-shifted gas (integrated over 18 km s^{-1} $\leqslant V_{\rm LSR} \leqslant 48$ km s^{-1}). The dashed rectangle indicates the extent of the mapped region, centered on $\alpha = 18^{\rm h}29^{\rm m}49\overset{\rm s}{.}7$, $\delta = 01^{\circ}15'22\overset{''}{.}8$ (J2000). Filled and dashed controus start at 0.8 K km s^{-1} with an 1 K km s^{-1} increment. HARP-B detector beam of $\sim$14″ is represented as a circle in the lower right corner. The dashed rectangle delineates the observed area, and solid rectangles named A, B, C represent areas that are presented in magnification in Figs. 3, 5, and 7 respectively.

dispersed (Kaas 1999). It has been suggested that the difference in the spatial distribution of YSOs at different evolutionary stages reflects different star-forming episodes in Serpens (Casali et al. 1993; Hurt & Barsony 1996; Kaas et al. 2004).

In Sects. 3.2–3.4, we examine the particular characteristics for each one of the defined areas A–C and attempt to attribute the observed outflows to individual sources. From this perspective, isolated outflows that are not comprised within the examined areas cannot be connected to any of the protostellar sources in the mapped area. High-velocity CO $J = 3 \rightarrow 2$ intensity maps are examined in conjuction with Spitzer IRAC band-2 (4.5 μm) and MIPS band-1 (24 μm) images from Winston et al. (2007). Within the IRAC band-2 that fall a number of high-excitation energy, pure rotational, and ro-vibrational H_2 lines that trace warm, shocked gas from the underlying protostellar jets, and such emission assists in the coupling between outflows and candidate driving sources. Possible connections are also derived by comparing with data from the very rich literature on Serpens, which covers observations of near-IR jets to high-density submillimeter, and millimeter molecular outflow tracers. From this analysis, we identify 11 sources that most likely are responsible for the bulk of molecular outflow activity observed in the Serpens Core. About half of these sources appear to drive bipolar outflows, and from these four exhibit H_2 jet-like emission associated with these outflows. The projected position angles of outflows which are estimated from the peaks of outflow emission with respect to the corresponding driving sources, tend to have, within uncertainties mainly due to the limited resolution of the maps, an orientation in the northwest-southeast direction (see Table 1 and Figs. 3, 5, and 7). This alignment has been attributed to the influence of the helical component of the large-scale magnetic field (Gomez de Castro et al. 1988); however, recent polarimetry observations (Sugitani et al. 2010) are indicative of a hourglass-shaped field centered between the northwest and southeast clumps, which in many cases is aligned perpendicularly to the direction of the observed outflows, therefore no

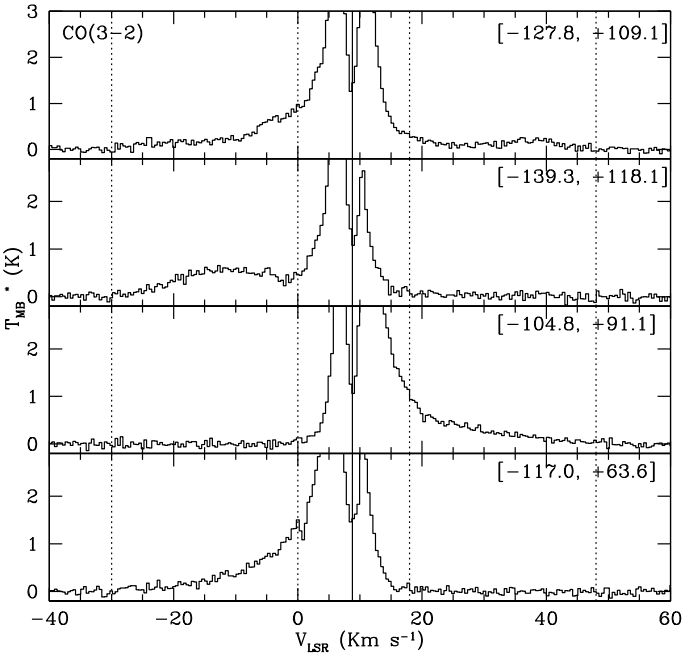

Fig. 2. CO $J = 3 \rightarrow 2$ spectra centered on the peaks of the high-velocity lobes of area B (see Fig. 1). Vertical scale is in units of corrected main beam brightness temperature, and map offsets are given in the upper-right corner of each spectrum. Dotted vertical lines mark the outer (−30, 48 km s^{-1}) and inner (0, 18 km s^{-1}) bounds over which we integrated the high-velocity blue-shifted and red-shifted emission; solid line marks the ambient cloud velocity ($V_{\rm LSR}$ = 8.8 km s^{-1}). In the lower two panels, high-velocity gas forms continuus, fading-off wings, whereas in the upper two panels high-velocity gas exhibits a semi-detached distribution with a secondary peak.

secure conclusions can be drawn from the present data on the role of the local magnetic field and the outflow alignment.

For the positional determination and characterization of the evolutionary state of the YSO's in the present study, we used the analytical catalogs of Winston et al. (2007). To avoid any confusion, we adopted the nomenclature of SMM sources listed in Casali et al. (1993), whereas for the rest we used the *Spitzer* ID from the Winston et al. (2007) catalog with the letter *W* as a prefix.

3.2. Area A

Figure 3 presents a magnification of the outflow activity within Area A (Fig. 1) superimposed on an IRAC band 2 (upper) and MIPS band 1 (lower) grayscale images while Fig. 4 shows individual velocity channel maps, which assisted in identifying the outflowing gas with respect to the ambient material and in associating blue- and red-shifted outflow lobe pairs emitted by the same source. In both panels of Fig. 3, the positions of known Class0/I sources from the catalog of Winston et al. (2007) are labeled along with prominent high-velocity outflow lobes. The extended blue-shifted emission in the south is discussed in the next section. Because it is located close to the border of the CO map, area A is not fully sampled. Contour levels employed here are the same as in Fig. 1 for the sake of consistency; however, outflows are better delineated in the velocity channel maps close to the low-velocity cutoffs of Fig. 4, where contour levels start at 0.25 K km s^{-1} and are spaced by the same amount.

Area A covers the S68N region to the northwest of the Serpens Core. Submillimeter single dish (Davis et al. 1999) and

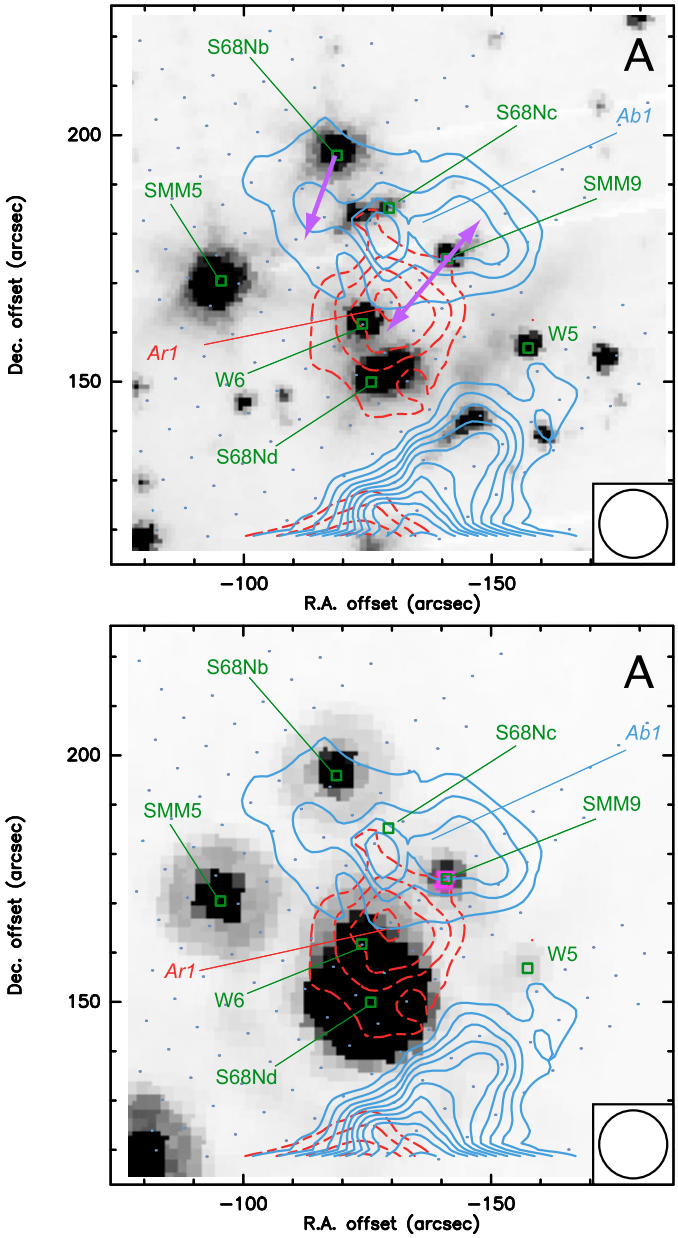

Fig. 3. Magnification of the high-velocity gas of Area A from Fig. 1 superimposed on an IRAC band 2 (*upper panel*) and MIPS band 1 (*lower panel*) images (in grayscale). In the *upper panel*, arrows indicate outflow axis and possible associations with protostellar sources. Contour levels are as in Fig. 1.

interferometric observations (Testi & Sargent 1998; Williams & Myers 2000) have revealed four cores, named S68Na through d, with S68Na most likely coinciding with the continuum source SMM9 (White et al. 1995; Wolf-Chase et al. 1998). To the east, the continuum source SMM5 (Casali et al. 1993) is possibly associated with the bright near-IR cometary nebula EC53 (Eiroa & Casali 1992; Hodapp 1999); however, while the head of the cometary nebula lies close to the submillimeter source, the latter is not detected in the near-IR.

The blue- and red-shifted lobes Ab1 and Ar1 in Fig. 3 most likely represent a bipolar outflow from S68Na/SMM9 at a projected position angle (PA) of ∼150°. Although at the far edge of the map Ab1 is not outlined well, the jet-like emission in the IRAC image adjacent to the driving source and pointing to the northeast possibly indicates the direction of the underlying jet,

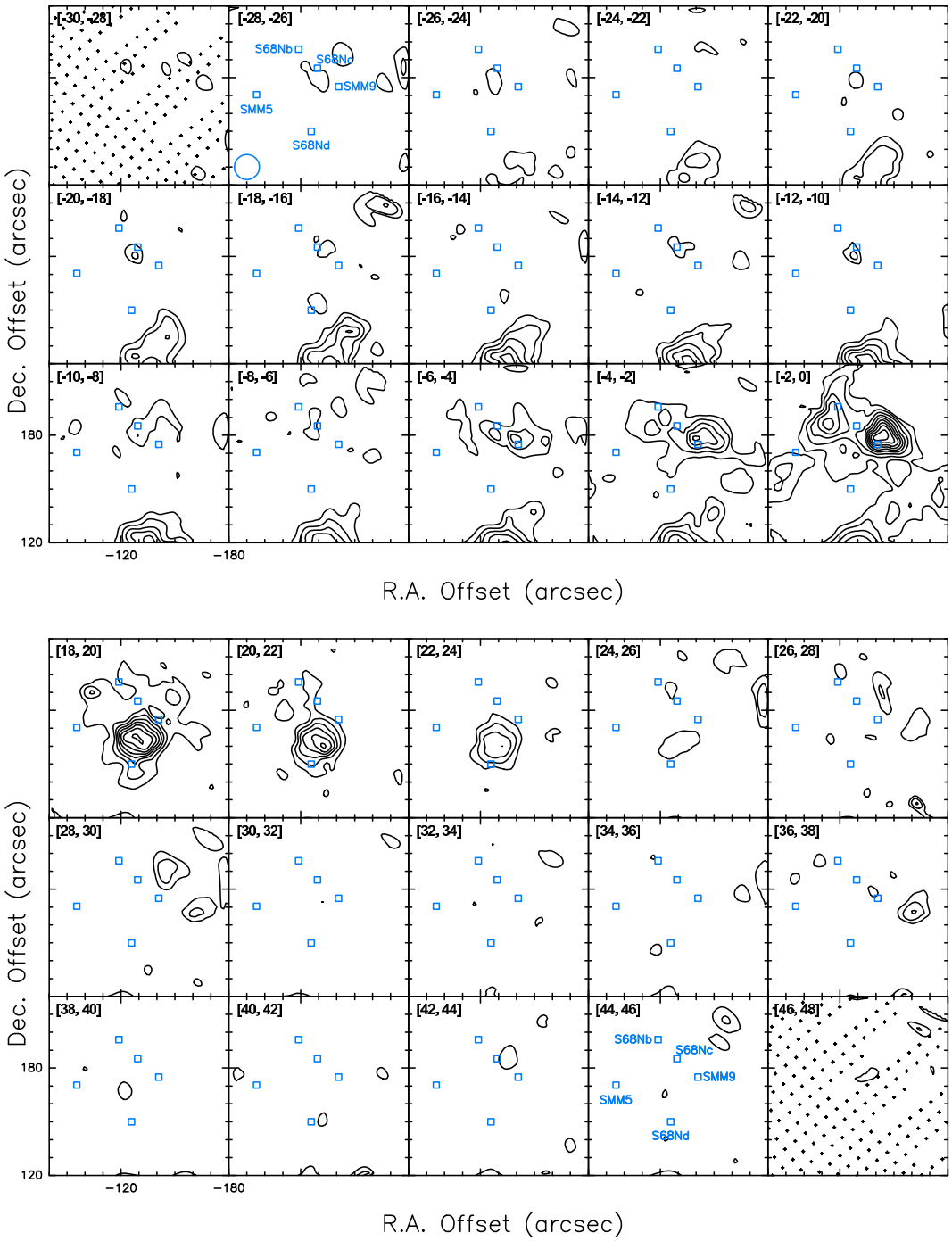

Fig. 4. Velocity channel map of area A (see Fig. 3). Each panel displays emission integrated over a 2 km s^{-1} interval, and contour levels start from 0.25 K km s^{-1} with a 0.25 K km s^{-1} increment. Crosses in the first and last panels display the sampling; the position of sources likely to drive outflows are displayed with empty squares.

which in this case coincides with the orientation of the associated outflow. Maps of CS $J = 2 \rightarrow 1$ (Wolf-Chase et al. 1998; Testi et al. 2000; Williams & Myers 2000), methanol (Testi et al. 2000; Garay et al. 2002), and SiO (Garay et al. 2002) outline a similar bipolar outflow connected to SMM9 at a position angle of ~135°–145° and therefore confirm this correlation.

The extension of lobe Ab1 to the east, roughly between S68Nb and SMM5, is harder to associate. The underlying jet-like emission in the IRAC image very close to S68Nc pointing to the southeast is resolved as a series of knots in near-IR H_2 1–0 $S(1)$ (2.12 μm) imaging (Hodapp 1999). Proper motions show that these knots are moving towards SMM5 (Hodapp 1999), hence favoring S68Nc as their progenitor. Still, it is doubtful if there exists an embedded protostar within the S68Nc clump, since it is scarcely detected in the far-IR and submillimeter continuum (Winston et al. 2007; Davis et al. 1999), and only appears as an elongated condensation at 3 millimeter. (Williams & Myers 2000). In the [−2, 0] velocity channel map of Fig. 4, Ab1 displays an orientation towards the south, implying a possible connection with S68Nb. Because other sources do not provide convincing evidence, we tentatively associate the extension of lobe Ab1 to the source S68Nb.

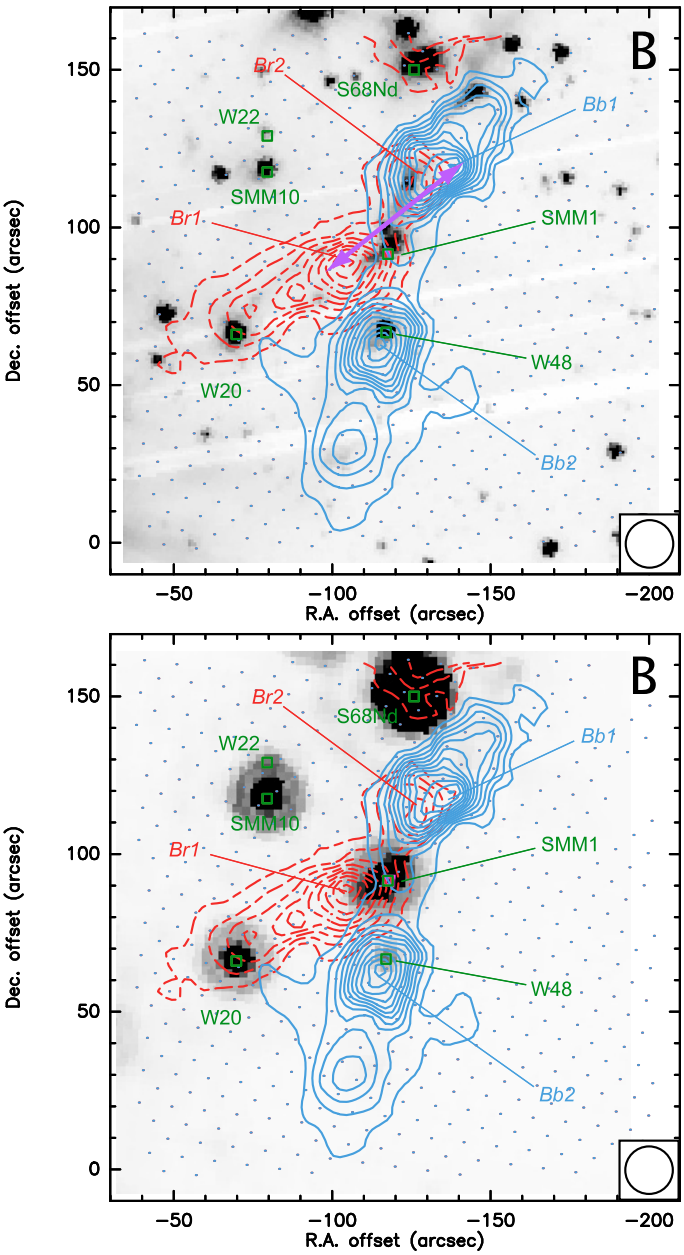

Fig. 5. Magnification of the high-velocity gas of Area B from Fig. 1 superimposed on an IRAC band 2 (*upper panel*) and MIPS band 1 (*lower panel*) images (in grayscale). Contour levels are as in Fig. 1.

In the [−2, 0] and [18, 20] channels of Fig. 4, two weak (blue- and red-shifted) lobes pointing to the southeast and northwest from SMM5 and possibly associated to this source are recorded. Owing to the contour level selection, these lobes are not visible in Fig. 3; however, we consider them as real and name them Ab2 and Ar2 (see Table 2). Similar weak red-shifted emission with roughly the same orientation is only recorded in the $J = 1 \rightarrow 0$ CO map of Narayanan et al. (2002).

3.3. Area B

Area B is located to the south of Area A and displays the outflow activity below the S68N clump. Although Areas A and B together confine the Serpens northwest region, due to its unique characteristics this segment is presented here as stand-alone. As in the case of Area A, in Fig. 5 we present high-velocity

Table 1. Outflow position angles.

Source	Outflow PA (°)
SMM1[a]	130 ± 5
SMM3[a]	155 ± 8
SMM4[a]	170 ± 7
SMM5[a]	135 ± 10
SMM6[b]	35 ± 8
SMM8[c]	...
SMM9[a]	150 ± 10
S68Nb[b]	160 ± 10
W10[b]	130 ± 8
W45[a]	70 ± 15
W48[c]	...

Notes. [(a)] Driving bipolar outflow. [(b)] Driving unipolar outflow. [(c)] Position angle uncetain.

$J = 3 \rightarrow 2$ CO outflows superimposed on the IRAC band 2 and MIPS band 1 images (upper and lower panels, respectively). Again, deeply embedded Class0/I sources are tagged along with the strongest outflow lobes.

This area comprises SMM1/FIRS1 and SMM10, with the former the most prominent source in Serpens (Casali et al. 1993; Hurt & Barsony 1996; Davis et al. 1999), which displays a series of mass-ejection phenomena. It has been associated with a radio jet and OH maser emission (Rodriguez et al. 1989; Curiel et al. 1993), while strong outflows have been traced in a number of molecular lines.

High-velocity CO emission, as shown in Fig. 5, is rather puzzling, because there are two blue-shifted (Bb1, 2) and two red-shifted lobes (Br1, 2) that all seem to converge towards SMM1. Both Bb1 and Br2 point out towards the northwest and overlap and the line wing morphology at the peaks of these lobes, presented in the upper two spectra of Fig. 2 indicates the existence of high-velocity "bullets", which in velocity channel maps of Fig. 6 can be traced up to the [−24, −22] and [+38, +40] velocity bins, symmetrically to the nominal cloud velocity. The spatial coincidence along with the common wing morphology, suggests that Bb1 and Br2 represent the same high-velocity gas projected at different Doppler shifts on the plane of the sky.

Mid-IR IRAC emission in Fig. 5 shows arc-shaped features, extending to the northwest and southeast outlining the rim of the CO lobes Bb1 and Br1. The same morphology is also traced in near-IR 1–0 S(1) H_2 imaging (Hodapp 1999) and possibly in CS (Williams & Myers 2000). Unlike the outflow from SMM9, the CS features corresponding to Bb1 and Br1 have opposite Doppler shift to the CO lobes and are much weaker. The base of the northwest and southeast cavities very close to SMM1 also appear in high-density molecular tracers such as HCO^+ and HCN (Hogerheijde et al. 1999) and the (1, 1) transition of ammonia (Torrelles et al. 1992).

All the existing evidence leads to the association of Bb1 and Br2 pointing to the northwest and Br1 to the southeast with SMM1 at a single bipolar outflow configuration; however, more complex configurations involving a binary source (as suggested by White et al. 1995) cannot be excluded. The position angle of the outflow is ∼130°, coinciding with the position angle of ∼125° of the underlying radio jet (Rodriguez et al. 1989; Curiel et al. 1993), which confirms the possible connection between the two phenomena. To the south, the alignment of the peak of lobe Bb2 with the flat spectrum source W48 (Winston et al. 2007) may be interpreted as if Bb2 is a face-on unipolar outflow with

Table 2. Outflow properties, for the blue- (integrated over $-30\ \mathrm{km\,s^{-1}} \leqslant V_{\mathrm{LSR}} \leqslant 0\ \mathrm{km\,s^{-1}}$) and red-shifted (integrated over $18\ \mathrm{km\,s^{-1}} \leqslant V_{\mathrm{LSR}} \leqslant 48\ \mathrm{km\,s^{-1}}$) gas.

Outflow	Source	N_{tot} (10^{16} cm^{-2})	M_{tot} ($10^{-3}\ M_{\odot}$)	P_{tot} ($10^{-2}\ M_{\odot}$ km s^{-1})	E_{K} (10^{42} erg)	t_{dyn} (10^{3} years)	F_{CO} ($10^{-5}\ M_{\odot}$ km s^{-1} yr^{-1})	L_{mech} ($10^{-2}\ L_{\odot}$)
				Area A				
Ab1	SMM9	1.89–2.97	0.49–0.78	1.03–1.63	1.25–1.98	0.7	1.47–2.33	1.42–2.26
Ar1	SMM9	1.87–2.95	0.48–0.77	1.10–1.72	0.73–1.16	0.9	1.22–1.72	0.64–1.03
Ab2	SMM5	1.53–2.41	0.4–0.63	0.3–0.49	0.24–0.4	2.9	0.11–0.17	0.07–0.11
Ar2	SMM5	1.07–1.7	0.3–0.45	0.23–0.37	0.2–0.32	1.5	0.15–0.24	0.11–0.17
Ab3	S68Nb	2.49–3.94	0.6–1.03	0.5–0.8	0.41–0.65	1.8	0.27–0.44	0.18–0.29
				Area B				
Bb1	SMM1	10.44–16.52	2.73–4.33	5.64–8.92	10.78–17.04	2.6	2.57–3.43	3.31–5.24
Br1	SMM1	8.62–13.63	2.26–3.57	4.22–6.67	6.23–9.85	2.9	1.45–2.30	1.71–2.71
Br2	SMM1	1.86–2.94	0.49–0.77	1.23–1.95	2.42–3.82	1.5	0.81–1.30	1.29–2.03
Bb2[a]	W48	10.02–15.84	2.62–4.15	4.36–6.89	5.97–9.44	...	...	...
Bb2[b]	W48	7.47–11.81	1.96–3.09	3.28–5.19	5.05–7.98	...	...	...
				Area C				
Cb1	SMM3	3.27–5.17	0.86–1.35	1.29–2.04	1.64–2.59	1.1	1.17–1.85	1.17–1.88
Cr1	SMM3	0.68–1.08	0.18–0.28	0.42–0.66	0.60–0.94	0.9	0.47–0.73	0.53–0.83
Cb3	SMM4	7.45–11.79	1.95–3.09	2.96–4.68	3.78–5.97	0.7	4.24–6.7	4.32–6.82
Cr3	SMM4	2.04–3.22	0.53–0.84	1.07–1.69	0.82–1.29	1.5	0.70–0.79	0.43–0.62
Cb2	SMM6	4.52–7.15	1.18–1.87	2.21–3.49	4.02–6.36	0.6	3.69–5.82	5.36–8.48
Cr2	...	0.31–0.49	0.08–0.12	0.18–0.28	0.02–0.03	...	...	...
Cr5[a]	W10	4.77–7.54	1.25–1.97	2.30–3.63	1.74–2.76	2.8	0.82–1.29	0.49–0.78
Cr5[b]	W10	1.67–2.63	0.43–0.69	0.88–1.40	0.46–0.73	...	...	...
Cb4	W45	3.37–5.34	0.88–1.40	1.44–2.27	1.08–1.71	1.9	0.76–0.89	0.45–0.72
Cr4	W45	1.90–3.01	0.50–0.79	0.90–1.42	0.70–1.11	2.1	0.43–0.67	0.26–0.42
N1	SMM8	5.09–8.05	1.34– 2.1	1.11–1.7	0.96–1.51	1.4	0.79–1.21	0.55–0.86

Notes. Lower and upper limits correspond to calculations based on the two values adopted for $\tau = 0, 1$. [(a)] Extended lobe. [(b)] Primary lobe.

an undetected receding, red-shifted lobe pointing away from the observer.

Very little evidence of outflows exists in the vicinity of SMM10, traced only in the [−2, 0] channel of Fig. 6. The evolutionary stage of this protostellar source is uncertain. Eiroa et al. (2005) has classified it as a Class 0 source, but the significant emission recorded shortward 24 μm (Winston et al. 2007) and the lack of strong outflows indicate a more advanced protostellar stage.

3.4. Area C

Area C comprises the SE clump of the Serpens Core, a highly populated region where protostellar sources in various evolutionary stages are packed with bright near-IR nebulosities. Millimeter and submillimeter maps (Casali et al. 1993; Testi & Sargent 1998; Davis et al. 1999) reveal four significant condensations, named after Casali et al. (1993) as SMM2, SMM3, SMM4, and SMM6. In the near-IR, the bright Serpens Reflection Nebula (SRN) is associated with SVS20 and SVS2, the two brightest near-IR sources in the Serpens Core complex (Eiroa & Casali 1992).

As in the previous areas discussed above, the high-velocity CO $J = 3 \rightarrow 2$ outflows are displayed over the IRAC band 2 (upper) and MIPS band 1 (lower) panels in Fig. 7. The positions of the SMM sources, along with other Class0/I and flat spectrum sources from Winston et al. (2007), are marked in both panels. A high concentration of possible Class II sources and field stars is observed towards the southwest in the IRAC image, while significant emission from the reflection nebula is apparent towards the north and center of Area C, With the exception of SMM6, all other SMM sources do not appear bright on the 24 μm MIPS band. Outflow contours around SMM3, SMM4, and SMM6 are clustered, but display a number of peaks that are tagged in both panels of Fig. 7. The velocity range for the majority of the outflows in this area is lower than observed for the northwest clump (areas A and B) and significant blue-shifted and red-shifted emission is recorded up to [−10, −8] and [26, 28] km s^{-1} velocity bins respectively, with an exception for the blue-shifted lobe Cb2, which is observed up to the [−26, −24] km s^{-1} channel (Fig. 8).

With the exception of SMM2, all SMM sources in the region have associated CS and H_2CO emission counterparts (Mangum et al. 1996). However, it is not yet clear whether SMM2 harbors a protostellar source. Despite being observed as condensation in the submillimeter (Davis et al. 1999), it is scarcely or not at all traced in millimeter continuum observations (Testi & Sargent 1998; Hogerheijde et al. 1999). In addition, the two nearby mid-IR Class0/I sources W17 and W18 present in the 24 μm MIPS band (Winston et al. 2007) are offset from the 3 m position of SMM2 (Testi & Sargent 1998), and therefore not related to it. The lobe Cb4, located 20″ to southwest is most likely not related to SMM2 but with some of the more evolved sources to the southeast, possibly in a bipolar scheme with Cr4. Therefore, the absence of any apparent outflow emission in the vicinity is in favor of the view that SMM2 is a warm cloud condensation without an embedded source.

SMM3 is a millimeter/submillimeter continuum source located to the north of Area C; in the IRAC image, there is strong jet-like emission extending to the northwest from the source, at a position angle of 155° traced also in the near-IR H_2 1–0 S(1) line (Herbst et al. 1997; Eiroa et al. 1997). Most likely, the emissions observed to the same direction in HCO^+, HCN, SiO (Hogerheijde et al. 1999), and CS (Testi et al. 2000) trace the

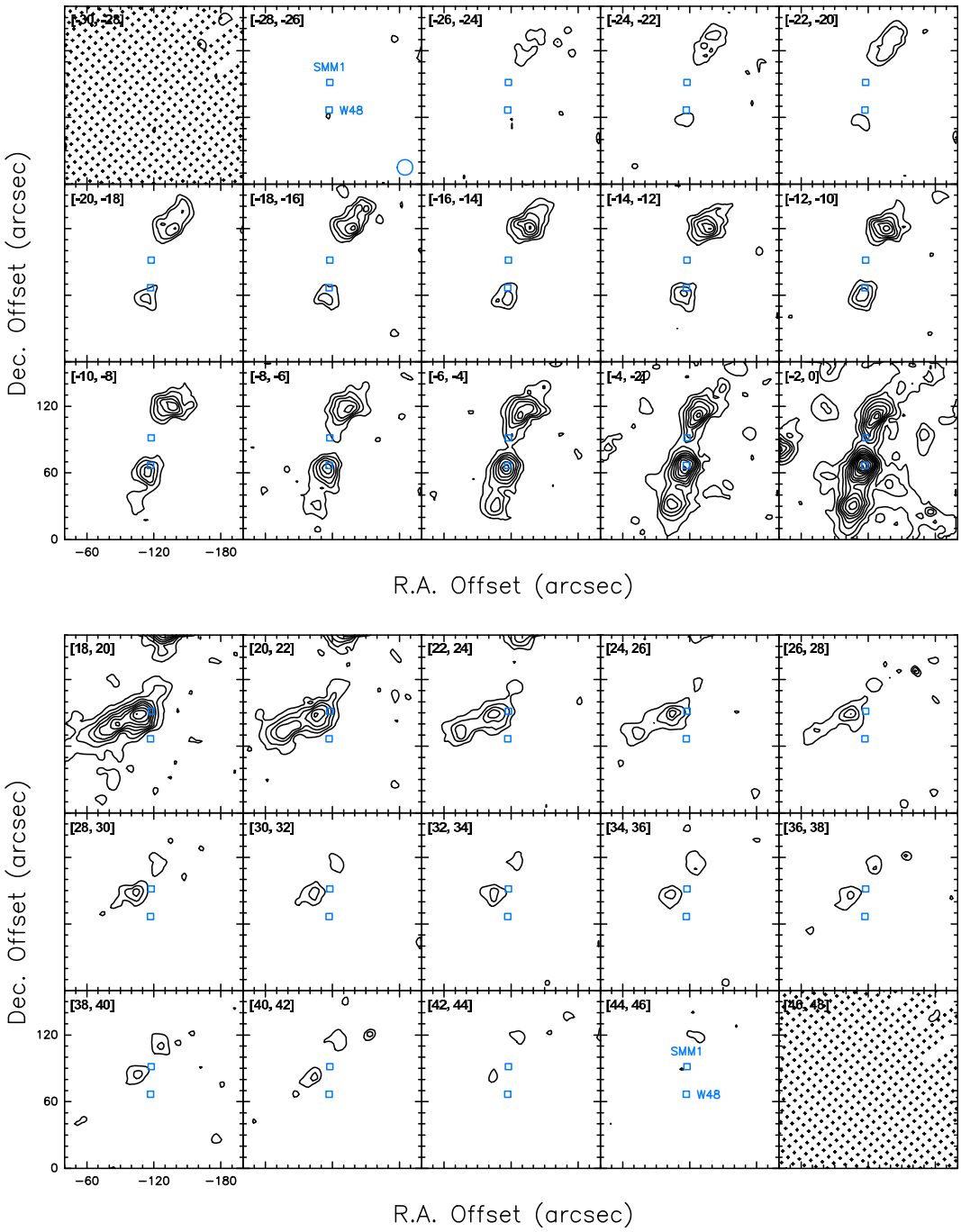

Fig. 6. As in Fig. 4, for the area B (see Fig. 5).

same outflow activity. Lobe Cb1 follows the direction of the jet-like emission and peaks ∼10″ to the northwest of SMM3, while Cr1 is collinear, pointing in the opposite southeast direction, and it peaks roughly at the same projected distance from the source. Even though a number of other nearby Class0/I sources (e.g. W19, W4) are present nearby, the positioning of SMM3 with respect to Cb1 and Cr1 along with the outflow detected in other molecular tracers favor their association.

SMM4 is located to the west in Fig. 7, between the two dominant diffuse emission regions in the IRAC image. In the same image, two small nebulosities appear very close to the source in a north-south direction. The same morphology is observed in the near-IR (Eiroa et al. 2005), while outflows with the same direction are traced in CS, CH_3OH (Testi et al. 2000), HCO^+, and HCN Hogerheijde et al. (1999), as well as in lower J CO maps (Davis et al. 1999; Narayanan et al. 2002). This structure becomes evident in the $J = 3 \rightarrow 2$ map of Narayanan et al. (2002) where a bipolar outflow is clearly shaped. In Fig. 7, lobes Cb3 and Cr3 display similar morphological characteristics, and most likely are associated with SMM4.

To the northwest of Area C, the bright IRAC nebulosity is at the location of the near-IR binary SVS20/EC90, the brightest near-IR source in Serpens (Eiroa & Casali 1992), coinciding with the position of millimeter/submillimeter source SMM6. This is a binary system is surrounded by a near-IR ring or nebulosity, with two spiral arms seen in opposite directions (Herbst et al. 1997; Eiroa et al. 1997), which have been interpreted as a circumbinary disk (Eiroa et al. 1997) or evacuated bipolar cavities (Huard et al. 1997). Binary components have a north-south distribution separated by only 1.5″, and both present a flat

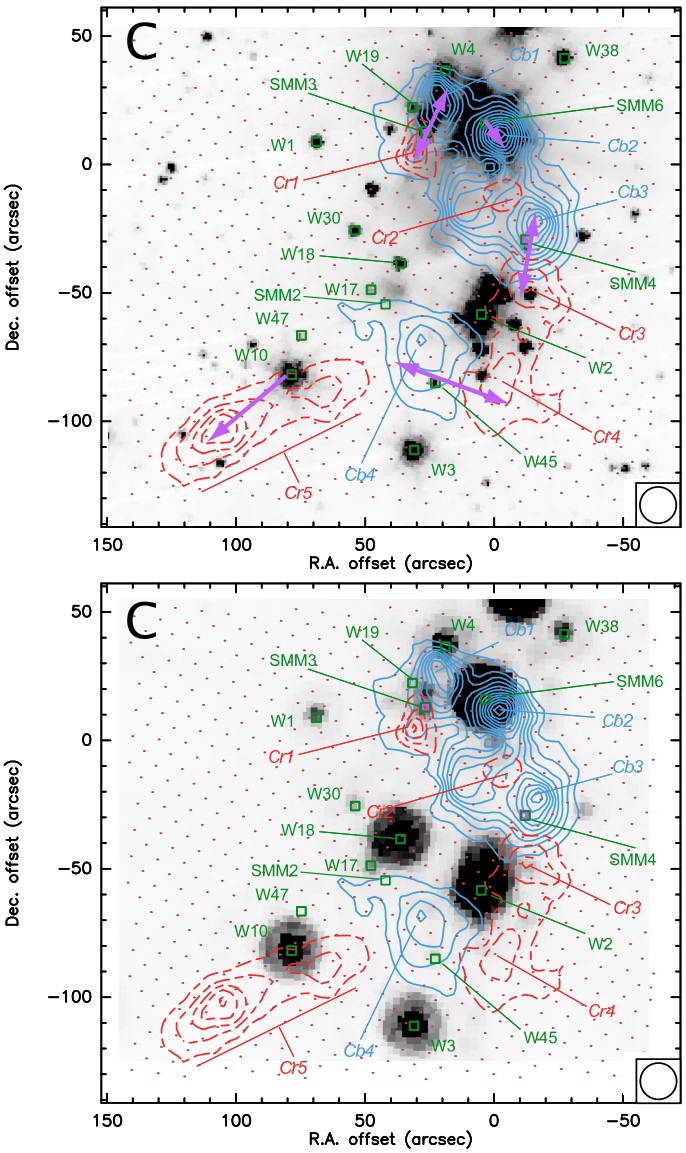

Fig. 7. Magnification of the high-velocity gas of Area C from Fig. 1 superimposed on an IRAC band 2 (*upper panel*) and MIPS band 1 (*lower panel*) images (in grayscale). Contour levels are as in Fig. 1.

spectrum SED (Haisch et al. 2002). It has been suggested that the southern component has strong Brγ and CO bands in emission indicating the presence of an accretion disk that most likely corresponds to SMM6 (Eiroa et al. 2005). The most prominent southern arm observed in the near-IR H_2 emission (Huard et al. 1997; Herbst et al. 1997; Eiroa et al. 1997) is in the direction of the blue-shifted lobe Cb2 in Fig. 7, and we tentatively attribute it to SMM6. Most likely, the red-shifted emission is obscured by the nebulosity, as A_V values ranging between 9 mag (Cambrésy 1999) and more than 20 mag (Huard et al. 1997) have been measured for this region.

To the south of Area C, there is a wealth of IRAC sources, the majority of them classified as Class II protostars or field stars. Class 0/I and flat spectrum sources from the Winston et al. (2007) catalog are labeled in Fig. 7, around lobes Cb4, Cr4, and Cr5. These lobes are present in lower J CO observations but are mostly prominent in the high-velocity map of Davis et al. (1999). The protostellar source W45 lying approximately between lobes Cb4 and Cr4 is a flat spectrum source (Winston et al. 2007) that could potentially drive the observed bipolar structure. Even though it is neither the least evolved nor the best positioned source with respect to the outflows, it is the only one that optimally satisfies both conditions. Similarly, the red-shifted lobe Cr5 is located just south of W10, classified as Class0/I in Winston et al. (2007) catalog which is possibly correlated to the bright continuum source PS2 detected by Hurt & Barsony (1996) and also present in the 3 mm map Testi & Sargent (1998). In the absence of any blue-shifted emission in the vicinity, we tentatively attribute Cr5 to W10 as a unipolar outflow.

Strong isolated red-shifted emission is evident in Fig. 1 to the north but outside of Area C in the vicinity of millimeter/submillimeter source SMM8. This emission corresponds to the northeast lobe of the high velocity CO map of Davis et al. (1999), and as in the case of W10, we tentatively correlate this emission to SMM8 as a unipolar outflow. Finally, no possible driving sources could be found for the remaining blue- and red-shifted lobes to the upper and lower left (east) of Area C in Fig. 1. We thoroughly examined the literature for a possible source between lobe Cr5 (Area C) and the intense blue-shifted emission outside the lower left corner of Area C which corresponds to lobe SEb in the high-velocity maps of Davis et al. (1999) which could justify a possible bipolar scheme, but no appropriate candidate sources could be found.

4. Outflow properties

In the following sections we calculate the fundamental outflow-related properties (i.e. column densities, masses, momentum, energies, momentum fluxes and mechanical luminosities), employing the method described in Choi et al. (1993) for the CO $J = 3 \rightarrow 2$ transition. Associated uncertainties are discussed in accordance with the present dataset and in respect with other methods (e.g. Cabrit & Bertout 1990; Bontemps et al. 1996; Fuller & Ladd 2002; Hatchell et al. 2007a).

4.1. CO column density and outflow mass

The column density in cm^{-2} per velocity channel i for the CO $J = 3 \rightarrow 2$ line was calculated from the relation

$$N_i^{\rm CO} = \frac{3h}{8\pi^3\mu^2} \frac{T^{\star}_{\rm MB(3-2)}\Delta V}{D(n,T_K)} \frac{\tau_{32}}{1-\exp(-\tau_{32})} \quad (1)$$

where μ is the dipole moment of the CO molecule, $T^{\star}_{\rm MB(3-2)}$ the corrected mean beam temperature in K within the velocity interval ΔV (in km s^{-1}), τ_{32} the optical depth, and $D(n,T_{\rm K})$ is given by the relation:

$$D(n,T) = f_2[J_\nu(T_{\rm ex}) - J_\nu(T_{\rm bk})][1-\exp(-h\nu/kT_{\rm ex})]. \quad (2)$$

Here, f_2 is the fraction of CO molecules in the $J = 2$ state, which is dependent on either temperature or the excitation conditions in the case of non-LTE, $J(T)$ is the Planck function in K, $T_{\rm ex}$ is the excitation temperature, and $T_{\rm bk} = 2.7$ K.

The particular characteristic of this method in deriving the column density as opposed to other methods introduced in the literature (e.g. Cabrit & Bertout 1990; Bontemps et al. 1996) lies in the treatment of the quantity $D(n,T)$. Cabrit & Bertout (1990) assume LTE conditions so that the excitation temperature equals the kinetic one; at this limit, $D(n,T)$ is independent of the density, so that $D(n,T) = D(T_{\rm K})$. Adopted kinetic temperatures in the literature vary from "cold" 10 K (10–20 K Cabrit & Bertout 1992; Bontemps et al. 1996) to "warm" (~50 K

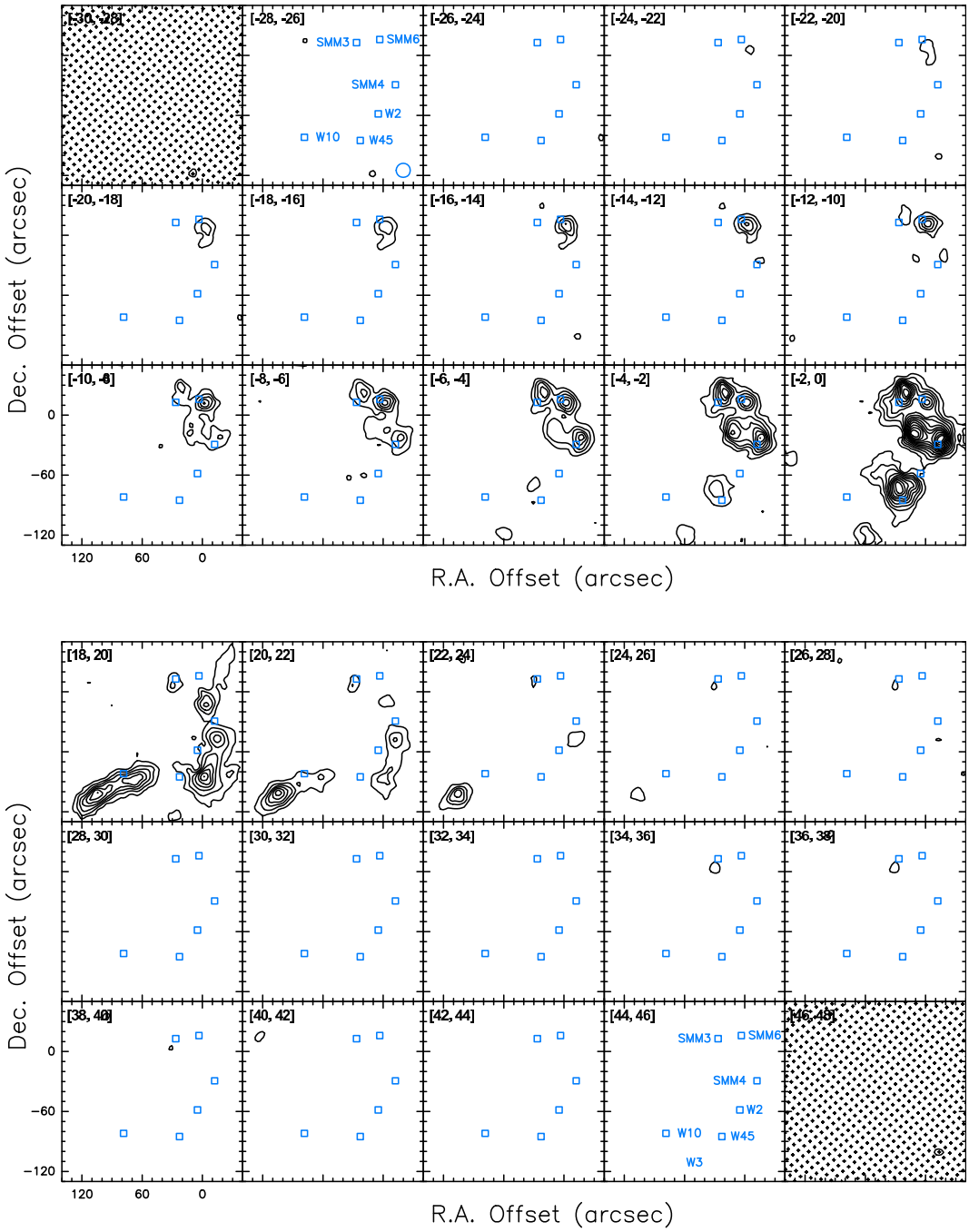

Fig. 8. As in Fig. 4, for the area C (see Fig. 7).

Hatchell et al. 2007a) CO gas, depending on the observed transition. Choi et al. (1993) approach this quantity in more general terms and assume non-LTE conditions. They employ LVG simulations to test its variance and find that an average value for $D(n, T_K) = 1.5$ is correct to less than a factor of 2 for the CO $J = 3 \rightarrow 2$ transition and for temperature ranging between 10 and 200 K and density from 10^4 to 10^6 cm^{-3}.

In the absence of isotopic CO observations for the HARP-B map that could provide means to independently estimate the optical depth, we assumed two values: $\tau = 1$ and the optically thin limit ($\tau = 0$). Although the $J = 3 \rightarrow 2$ CO line in the center is heavily self-reversed (see Fig. 2), for the high-velocity wings, optically thin emission is a reasonable assumption as White et al. (1995) find for the wings of the $J = 2 \rightarrow 1$ transition a CO/^{13}CO >20. This should be particularly true for $J = 3 \rightarrow 2$ line wings presented here that are more extended to higher velocities and integrated even farther from the body of the line.

We applied this method by summing for all data points enclosed within each of the individual lobes discussed in Sects. 3.2–3.4. Outflows were considered within velocity ranges -30 km s$^{-1} \leqslant V_{LSR} \leqslant 0$ km s^{-1} for the blue- and 18 km s$^{-1} \leqslant V_{LSR} \leqslant 48$ km s^{-1} for the red-shifted lobes and a velocity step of 1 km s^{-1} was used. The summed-up CO columns for each lobe are reported in Col. 2 of Table 2 for the two adopted values of τ.

The mass per channel M_i can be derived from the column density per channel (Eq. (1)) given the distance, D and the beam solid angle, Ω:

$$M_i = 2\,\mu m_H D^2 \Omega N_i^{CO} \frac{[H]}{[CO]} \quad (3)$$

Table 3. Global properties of the high-velocity gas.

	$M_{\rm tot}$ ($10^{-2}\ M_\odot$)	$P_{\rm tot}$ $10^{-1}\ M_\odot\ {\rm km\,s^{-1}}$)	$E_{\rm K,tot}$ (10^{43} erg)
Blue	1.12–1.76	1.97–3.04	2.92–4.55
Red	0.75–1.27	1.28–2.09	1.44–2.34
Sum	1.87–3.03	3.25–5.13	4.36–6.89

where $\mu = 1.3$ is the mean molecular mass and m_H the hydrogen atom mass. In Choi et al. (1993), the abundance ratio is separated into two terms with respect to carbon, and two different cases are taken for the [C]/[CO] ratio, one considering CO in swept-up gas and another one treating CO as an intrinsic jet ingredient. Following Choi et al. (1993), we consider a CO abundance ratio $X_{\rm CO} = 5\times10^{-5}$, under the assumption that the observed outflows are indeed swept-up ambient material. The estimated mass for individual lobes and the total mass for the blue and red high-velocity gas considering the two adopted values of τ are reported in Tables 2 and 3.

4.2. Momentum and energy

Once the mass per channel has been calculated for individual outflows, momentum and kinetic energy of each outflow can be derived from the following relations:

$$P = \sum_i M_i |V_i - V_0| \tag{4}$$

$$E_{\rm K} = \sum_i \frac{1}{2} M_i (V_i - V_0)^2 \tag{5}$$

where V_0 is the nominal cloud velocity, and sums act over velocity channels (i) reported above for the blue- and red-shifted lobes. The derived momentum and kinetic energy for each individual outflow are reported in Cols. 3 and 4 of Table 2. The total mass, momentum, and kinetic energy for the high-velocity blue- and red-shifted gas in the Serpens Core are listed in Table 3; in all cases, lower and upper limits reflect the assumption of the two different values for τ.

The total mass estimates lie between 1.9 and $3.0\times10^{-2}\ M_\odot$, for the momentum between 3.25 and $5.1\times10^{-1}\ M_\odot\,{\rm km\,s^{-1}}$ and energy from 4.4–6.9×10^{43} erg. Total values of these properties for the blue-shifted gas are 50% higher than for the red-shifted emission. In comparison to the global outflow mass, momentum, and energy for the CO $J = 2 \rightarrow 1$ high-velocity gas reported in White et al. (1995) and Davis et al. (1999), our estimations are 1–2 orders of magnitude lower. For comparison, integrating over the velocity intervals considered in Davis et al. (1999) ([−4, 4] km s^{-1} and [14, 22] km s^{-1} for the blue- and red-shifted gas) yields values that are an order of magnitude lower than the ones derived by the CO $J = 2 \rightarrow 1$. Part of this difference could come from the much larger area of $720'' \times 560''$ considered in Davis et al. (1999) than the area of the present maps ($460'' \times 230''$). Indeed, considering the velocity limits used in Graves et al. (2010) ([−15, 6] km s^{-1} and [10, 30] km s^{-1} for the blue- and red-shifted gas), our estimates are less than a factor of two lower. Also the outflow masses and momenta for individual outflows reported in Table 3 of Graves et al. (2010) are within a factor of two of the ones reported in Table 2. Such a difference can easily come from the different adopted methods for measuring these quantities.

4.3. Momentum flux and mechanical luminosity

The driving force of the underlying stellar wind or jet should correspond to the average force applied to the outflow gas. Its magnitude can be estimated if the momentum of the outflowing gas is divided by the characteristic flow time-scale $t_{\rm ch}$:

$$F_{\rm CO}^{\rm obs} = \frac{P}{t_{\rm ch}}\,. \tag{6}$$

The characteristic timescale is defined as the maximum projected radius that the flow has covered R, over the mass weighted velocity of the flow $v_{\rm ch} = P/M$, This timescale represents a lower limit as it is not corrected for any possible inclination of the outflow. In addition, most swept up mass in jet-driven shocks is located in the bow wings and moves much more slowly than material in the bow-head; therefore the mass weighted velocity may contribute in underestimating outflow ages (Downes & Cabrit 2007). Thus $F_{\rm CO}$ becomes:

$$F_{\rm CO}^{\rm obs} = \frac{P^2}{MR}\,. \tag{7}$$

Inclination of the outflow with respect to the plane of the sky will lead in underestimating the true outflow length and the characteristic velocity. Adjusting for the inclination effects on the observed momentum flux yields:

$$F_{\rm CO} = \frac{P^2}{MR} \times \frac{\sin(i)}{\cos^2(i)}, \tag{8}$$

where i is the angle between the flow axis and the line of sight. As the latter quantity cannot be inferred from the existing data on an individual outflow basis, we assumed an arbitrary inclination angle $i = 45^\circ$ for all outflows corresponding to an inclination correction factor of 1.41. In a similar manner, the total energy from the jet deposited on the ambient gas can be derived by dividing the outflow energy by the characteristic timescale,

$$L_{\rm mech}^{\rm obs} = \frac{E_{\rm K}}{t_{\rm ch}}\,. \tag{9}$$

The inclination taken into account corresponds to a factor of $\sin(i)/\cos^3(i)$, which results in a correction factor of 2 for an angle of 45°. The derived momentum fluxes and mechanical luminosities for each individual outflow are reported in Table 2.

Results from numerical simulations of outflows (Downes & Cabrit 2007) argue that the characteristic timescale $t_{\rm ch}$ as defined above will overestimate the true outflow length, as mass-weighted velocities underestimate the true propagation speed of the bow-shock head, which defines its actual length in a jet driven outflow. Other factors, such as the role of the transverse momentum and the dissociation of CO molecules at bowshocks, may affect the estimations of momentum flux to a greater or lesser extent (for a complete discussion we refer the interested reader to Downes & Cabrit 2007). However, deriving of the momentum flux based on the maximum velocity as suggested by Downes & Cabrit (2007) may lead to more uncertain results, since $v_{\rm max}$ is more affected by the inclination of the outflow. Furthermore, this method may give misleading results in the presence of high-velocity "bullets", as is the case in a number of outflows in the present sample. In our method for deriving the momentum flux, overestimating the true outflow age is compensated for to an extent by the high $v_{\rm min}$ cutoffs adopted for the outflows; for example, assuming $v_{\rm min}$ values closer to $v_{\rm LSR}$ by 4 km s^{-1}, the mechanical energy increases by ∼15%. Characteristic timescales and momentum fluxes for each outflow

are reported in Table 2. There are two cases where the characteristic timescale could not be determined: for lobe Bb2, the outflow seems to be almost aligned with the line of sight from the driving source W48, while no possible driving source could be assigned to lobe Cr2 (see Sect. 3.4).

There are no studies where CO momentum fluxes are estimated for individual sources in Serpens. However, comparison with other studies shows that derived values presented in Table 2 are of the same order of magnitude as the ones in the case of Bontemps et al. (1996) examining a sample of 45 low-luminosity embedded young stellar objects, and 2 orders of magnitude higher than to the lower limits inferred by Hatchell et al. (2007a) for a sample of embedded sources in Perseus cloud. There is a factor of ∼10 implied by the opacity and inclination corrections implemented in the momentum fluxes of Bontemps et al. (1996) that are not considered by Hatchell et al. (2007a). Even corrected for this factor, there is an order of magnitude discrepancy even for the outflows attributed to the same sources in the two studies, which reflects the high uncertainties in the momentum flux calculations.

Based on the observed CS outflow associated with S68N/SMM9 core, Wolf-Chase et al. (1998) estimated a momentum flux $F_{\rm CO} \sim 2 \times 10^{-4}\ M_\odot\,{\rm km\,s^{-1}\,yr^{-1}}$. This is an order of magnitude higher than the sum of the lobes Ar1 and Ab1, which are attributed to SMM9 in our study. Even though the SMM9 outflow being at the edge of out map is not fully sampled, the value derived by Wolf-Chase et al. (1998) is still high as it corresponds to the total momentum flux for the whole Serpens core in the optically thin limit ($\sim$2.8–5 $\times 10^{-4}\ M_\odot\,{\rm km\,s^{-1}\,yr^{-1}}$). A series of factors including the assumed dynamical timescale along with the low-velocity cutoffs (which go deeply into the body of the CS lines in Wolf-Chase et al. 1998) may explain this discrepancy most easily. It should also be noted that the relatively high CS abundance employed in Wolf-Chase et al. (1998) is expected to lower the momentum flux (see Eq. (3)); however, the CS abundance is highly uncertain so the comparison between CO and CS derived momentum fluxes is not straightforward. The total momentum flux estimated by Davis et al. (1999) for all the outflows in Serpens, ($\sim 3 \times 10^{-4}\ M_\odot\,{\rm km\,s^{-1}\,yr^{-1}}$) is in good agreement with our measurements. However, in this case, the ∼10 times higher outflow momentum (see Sect. 4.2) estimated in Davis et al. (1999) is balanced by an equally overestimated average characteristic timescale (3×10^4 yr), due to the low values of the assumed maximum gas velocity and the extended typical length estimated for the outflows.

4.4. Bolometric luminosity

The spectral energy distribution (SED) of very young, embedded Class0/I sources spans a wavelength range from the near or mid-IR to millimeter and centimeter wavelengths; typically, the observed flux density is low in the near and mid-IR, while it peaks in the far-IR as the reprocessed protostellar flux is emitted by the massive surrounding envelope, falling back to lower values at longer wavelengths (Enoch et al. 2009).

Estimations of the bolometric luminosity for the very young protostars in the Serpens core differ substantially in diverse studies (Casali et al. 1993; Hurt & Barsony 1996; Larsson et al. 2000). In particular, the large beams of the mid and far-IR facilities deployed (e.g. *IRAS*; Hurt & Barsony 1996, and *ISO*; Larsson et al. 2000) do not posses enough spatial-resolving power to resolve the emissions from the highly clustered YSOs in the Serpens core. This leads to overestimated SED peak values for very young protostars and consequently to higher bolometric luminosities. Indeed, recent calculations based on *Spitzer* far-IR data which have an improved spatial resolution, Enoch et al. (2009) find $L_{\rm bol}$ values up to an order of magnitude lower than previous studies.

Here, we estimate bolometric luminosities for the sources that are likely to be responsible for the observed outflow activity, compiling data extending from the mid and far-IR (Winston et al. 2007; Harvey et al. 2007), 450 and 850 μm in the submillimeter (Davis et al. 1999), 1.1 and 3 mm (Enoch et al. 2007; Williams & Myers 2000) to 3.5 cm (Eiroa et al. 2005) observations of the Serpens core. The Spitzer mid- and far-IR photometry reported in the two independent studies of Winston et al. (2007) and Harvey et al. (2007) are in good agreement except for the 70 μm MIPS band, where values reported by Harvey et al. (2007) are always higher by a factor between 2 and 3. As the bulk of the derived bolometric luminosity rises from the area where flux density peaks (i.e. the far-IR for Class 0 sources), the 70 μm flux plays a dominant role. We therefore estimate upper and lower $L_{\rm bol}$ limits, taking the two independent Spitzer datasets into account. Spectral energy distribution diagrams for the Winston et al. (2007) catalog sources exhibiting 70 μm emission along with flux densities estimated in Harvey et al. (2007) are presented in Fig. 9.

Flux density in the SEDs is sampled over a wide range of wavelengths with a small collection of data points. Before integrating, we use a simple linear interpolation method similar to the "mid-point" method employed by Enoch et al. (2009). However, while a single interpolant is used in the "mid-point" method, in our calculations instead interpolants are introduced over a constant wavelength step of 5 μm. Upper and lower limit bolometric luminosities obtained with this method for the adopted distance of 310 pc are reported in Table 4.

The derived bolometric luminosities agree closely with the ones reported in Enoch et al. (2009), despite the different assumptions and methods. The $L_{\rm bol}$ upper and lower limits in Enoch et al. (2009) are estimated by means of two different integration methods (see Appendix A in Enoch et al. 2009) considering only the *c2d* survey dataset of Harvey et al. (2007) and assuming a 260 pc distance to Serpens. It should be noted, however, that peak fluxes are interpolated over in the "mid-point" method, so that the dominant influence of the 70 μm band is lost. Thus in principle, the bolometric luminosities estimated here and in the case of Enoch et al. (2009) should differ by a factor of $(310)^2/(260)^2 \sim 1.4$ due to the different adopted distances. Thorough tests on the same dataset of the two integration methods have shown that the predicted bolometric luminosities depend strongly on the number of interpolants between the observed points, and the estimated values are lower by a factor of ∼1.5 compared to the single interpolant adopted by Enoch et al. (2009), canceling the difference in the adopted distances.

In Table 4 we also report the ratio of the submillimeter (>350 μm) to the bolometric luminosity, for the sources having enough observed submillimeter and millimeter data points . This ratio being greater than 0.5% is indicative of the envelope mass exceeding the central stellar mass, therefore distinguishing between Class 0 and more evolved protostars (Andre et al. 1993). Associated errors are estimated considering the different values reported in the two mid/far IR studies with *Spitzer* (Winston et al. 2007; Harvey et al. 2007). Four protostellar sources, namely SMM1, SMM3, SMM4, and SMM9, fulfill this criterion and therefore are candidate Class 0 protostars in Serpens. We stress, however, that this ratio is dependent on the physical and observed properties of a particular source such as the inclination of outflow cavity with respect to the line-of-sight,

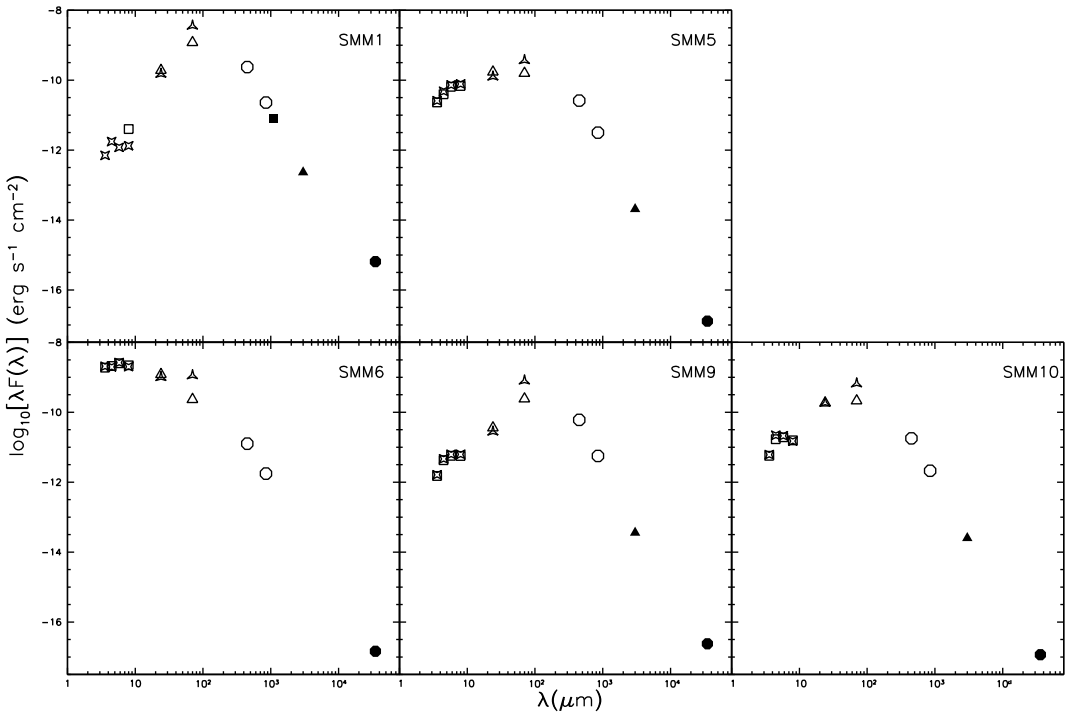

Fig. 9. Spectral energy distribution diagrams for the sources exhibiting 70 μm emission. Empty squares and star-like squares are IRAC band 1 to 4 flux densities from Winston et al. (2007) and Harvey et al. (2007) respectively; empty triangles and star-like triangles are MIPS band 1 and 2 from Winston et al. (2007) and Harvey et al. (2007). Empty circles are submillimeter flux densities at 450 and 850 μm from Davis et al. (1999). Filled squares and triangles are 1.1 and 3 mm flux densities from Enoch et al. (2007) and Williams & Myers (2000). Filled circles are 3.5 cm flux densities from Eiroa et al. (2005). Note that the 70 μm flux of Harvey et al. (2007) is constantly higher by a factor ∼2–3 compared to the one reported by Winston et al. (2007).

Table 4. Momentum flux and bolometric luminosity.

Source	$L_{\rm bol}{}^a$ ($L_\odot$)	$M_{\rm CO}$ (10^{-3} $M_\odot$)	$F_{\rm CO}{}^b$ (10^{-5} $M_\odot$ km s^{-1} yr^{-1})	$L_{\rm mech}{}^b$ (10^{-2} $L_\odot$)	$L_{\rm smm}/L_{\rm bol}$ (10^{-2})
SMM1	7.7 ± 2.4	6.45 ± 1.45	6.48 ± 3.24	12.96 ± 2.92	4.4 ± 0.9
SMM3	1.05 ± 0.5	1.33 ± 0.3	3.04 ± 1.23	4.42 ± 1.0	5.8 ± 1.1
SMM4	0.25 ± 0.05	3.2 ± 0.72	9.03 ± 2.01	12.24 ± 2,74	4.8 ± 0.8
SMM5	1.62 ± 0.22	0.89 ± 0.19	0.47 ± 0.11	0.46 ± 0.1	0.3 ± 0.1
SMM6	13.54 ± 0.8	1.52 ± 0.34	6.71 ± 1.5	13.84 ± 3.12	0.2 ± 0.1
SMM8	0.068	1.72 ± 0.38	1.41 ± 0.29	1.4 ± 0.3	···
SMM9	1.73 ± 0.3	1.26 ± 0.29	4.43 ± 1.28	5.34 ± 1.22	5.8 ± 0.7
W45	0.027	1.78 ± 0.40	1.95 ± 0.26	1.84 ± 0.42	···
W10	2.10 ± 0.1	2.17 ± 0.49	1.49 ± 0.33	1.26 ± 0.28	···
S68Nb	0.47	0.95 ± 0.35	0.55 ± 0.12	0.46 ± 0.1	0.2 ± 0.1

Notes. $^{(a)}$ Lower and upper limits based on Spitzer data from Winston et al. (2007) and Harvey et al. (2007). $^{(b)}$ Values corrected for inclination angle $i = 45°$.

therefore it only may provide indications and not constraints on the evolutionary stage of a protostellar source.

5. Discussion

5.1. Outflow momentum flux and mechanical luminosity versus bolometric luminosity relations

We examine the well-known correlation between momentum flux and bolometric luminosity that has been proposed by Cabrit & Bertout (1992) and Bontemps et al. (1996) for the homogenous sample of young protostellar objects in the Serpens Core. The outflow momentum flux $F_{\rm CO}$ is plotted against the bolometric luminosity $L_{\rm bol}$ in the upper panel of Fig. 10. Empty circles correspond to Serpens sources with associated outflows that both quantities could be determined, with error bars displaying the corresponding uncertainties discussed n the previous sections. Arrows and asterisks correspond to sources/outflows that either $F_{\rm CO}$, $L_{\rm bol}$ or both are uncertain. The dashed and dot-dashed lines display the location for the Class I correlation of Bontemps et al. (1996) and the relation for a sample of both low and high mass protostellar sources of Wu et al. (2004).

All protostellar sources found to have a high submillimeter to bolometric luminosity ratios stand well above of both Bontemps et al. (1996) and Wu et al. (2004) correlations. In addition, Class 0 and I sources are distributed above and below the Wu et al. (2004) correlation, which derived for a large sample of both low and high mass protostars. The placement of Class 0 sources confirms the soundness of our estimations, as the Wu et al. (2004) relation is strongly affected by high mass protostars, which are expected to have short evolutionary times and

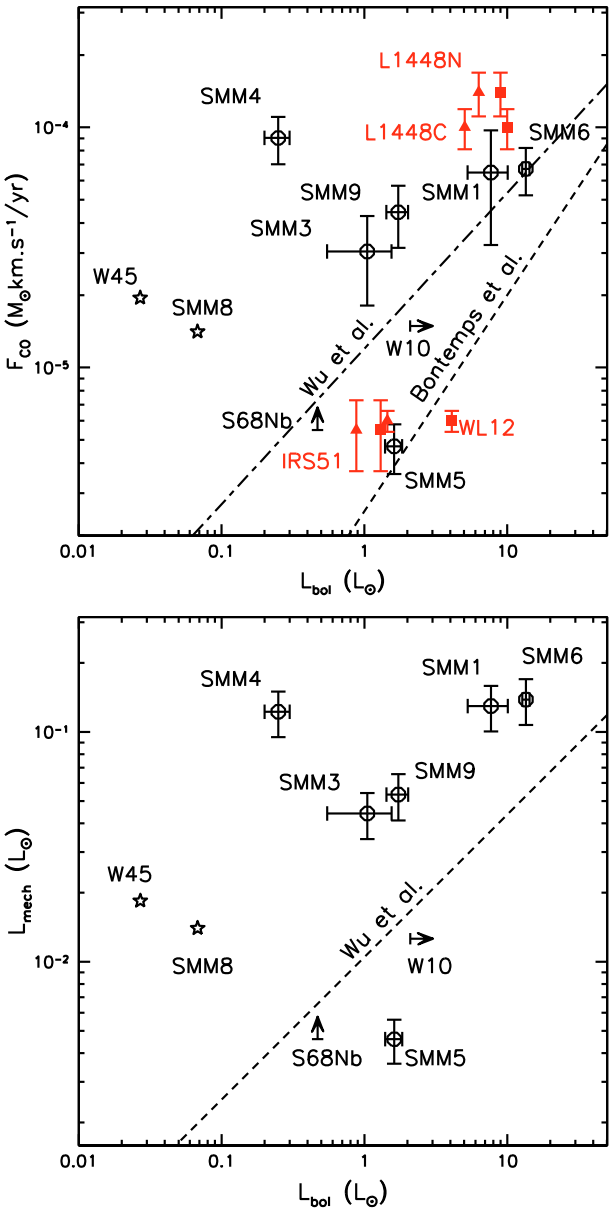

Fig. 10. (*Upper panel*) Momentum flux vs bolometric luminosity. Open circles indicate sources from the current sample of Serpens, vertical errorbars correspond to values of the momentum flux for $\tau = 0$ and 1, and horizontal errorbars to the differences in the derived bolometric luminosities for the different Spitzer fluxes in Winston et al. (2007) and Harvey. Arrows and asterisks mark Serpens sources that either F_{CO}, L_{bol}, or both are uncertain. The dashed line shows the location of the Class I correlation of Bontemps et al. (1996), and the dot-dashed line the correlation of both low- and high-mass sources of Wu et al. (2004). Filled (red) squares correspond to test sources from the sample that Bontemps et al. (1996) used to control the influence of the new Spitzer derived (red triangles) L_{bol} to the correlation. (*Lower panel*) Outflow mechanical luminosity versus the bolometric luminosity for the sample of sources in Serpens; the $L_{mech} - L_{bol}$ correlation for the sample of both low- and high- mass sources of Wu et al. (2004) is shown as a dashed line, running through the data points and separating Class 0 and Class I sources.

therefore are expected to be older than the low mass Class 0 protostars.

While the sample of Class I sources is not large enough to drive statistically significant conclusions, it appears that Class I sources are shifted to lower luminosities with respect to what is predicted from the correlation of Bontemps et al. (1996). This shift should not come as a surprise, since bolometric luminosities reported in this work and in Enoch et al. (2009) are up to a factor of ~10 lower than previous estimations (Casali et al. 1993; Hurt & Barsony 1996; Larsson et al. 2000), this difference being attributed to the better spatial resolution of *Spitzer*.

In order to explore the effect of the updated bolometric luminosities on the Class I correlation, we have selected four additional sources from the Bontemps et al. (1996) sample, since the latter contains no sources belonging to Serpens that could be used for direct comparison. From these, L1448C and N are bonafide Class 0 protostars in Perseus and their SEDs were determined using Spitzer photometry (Jørgensen et al. 2006; Rebull et al. 2007) and submillimeter/millimeter observations (Hatchell et al. 2007b; Enoch et al. 2006). The other two (IRS51 and WL12) are characterized as Class I sources (Bontemps et al. 1996) located in Ophiuchus, and for their SEDs we have compiled observations from Spitzer (c2d database, Evans et al. 2003; Padgett et al. 2008), and submillimeter/millimeter (Johnstone et al. 2000; Stanke et al. 2006). In Fig. 10, data points for these four sources as originally reported in Bontemps et al. (1996) (filled squares) are brighter by a factor between 2 and 3 than the bolometric luminosities based on Spitzer data (filled triangles). Despite this shift, Class I sources IRS51 and WL12 are roughly in the same part of the diagram with Class I candidates from the Serpens sample; the corresponding shift for the Class 0 sources places them even further from the Class I correlation, so that a decline in momentum flux from the Class 0 to the Class I phase is preserved. In another, uniform sample survey of Perseus, Hatchell et al. (2007a) found a less clear separation for the two classes; however, in the Serpens sample, all confirmed Class 0 sources seem to be standing well off the Class I group. With the exception of SMM4, all SMM1, SMM3, and SMM9 together with Perseus Class 0 sources seem to be well aligned indicating higher CO thrust than the Class I case (an order of magnitude for $L_{bol} = 1\ L_\odot$). Hints of a possible alignment between these Class 0 sources exists, however a larger sample of protostellar sources would be necessary to confirm it. To this direction, the HARP-B CO $J = 3 \rightarrow 2$ maps of Perseus (Hatchell & Dunham 2009) along with the existing *Spitzer* and submillimeter/millimeter surveys of the region combined with the present data would be an ideal dataset for probing this possibility.

Extending the investigation of the relations between outflows and the driving sources in Serpens, in the lower panel of Fig. 10 we plot the mechanical luminosity (L_{mech}) of the outflows versus the bolometric luminosity (L_{bol}) of the corresponding protostellar sources. The corresponding correlation of Wu et al. (2004) comprising both low- and high-mass protostars is indicated by a dashed line. The distribution of data points is similar to the F_{CO} vs. L_{bol} in the upper panel of the same figure and is consistent with the data distribution of Wu et al. (2004). Similarly, Class 0 sources stand well above the Wu et al. (2004) correlation; this is not unexpected, as the Wu et al. (2004) correlation is derived for a large sample of sources spanning different masses and ages. Despite the sample's limitations, it appears that sources with high bolometric luminosities tend to produce outflows with relatively lower mechanical luminosity than the sources having lower bolometric luminosities, and a similar behavior may also be observed in the sample of (Wu et al. 2004).

6. Summary and conclusions

We carried out CO $J = 3 \rightarrow 2$ observations, of the Serpens Cloud Core with the HARP-B detector on JCMT, covering an area of $460'' \times 230''$. These higher J CO observations along with

the higher sensitivity of the HARP-B, have allowed a sharp delineation of the outflow activity in Serpens, which enabled the association of individual outflows with protostellar sources to a greater extent than before. Such associations were aided by comparing them with other jet/outflow tracers, performed in other studies in the literature, and have resulted in associating most observed outflows to ∼10 protostellar sources. The projected orientation on the plane of the sky for the majority of the outflows, displays a preference for the northwest-southeast direction. This orientation is roughly parallel to the local galactic magnetic field as predicted by magnetically controlled cloud collapse models. For individual outflows, deduced column densities, masses and kinematical and dynamical properties are in good agreement with previous studies. However, estimated bolometric luminosities based on Spitzer mid and far-IR observations are up to a factor of 10 lower than previous estimations based on *IRAS/ISO* data. This difference is reflected as a possible shift in the $F_{\rm CO}$ vs. $L_{\rm bol}$ Class I correlation of Bontemps et al. (1996) to lower luminosities. Nontheless, the distribution of Class I sources remains separated from the one of Class 0 protostars. Indications of an independent $F_{\rm CO} - L_{\rm bol}$ correlation for the latter sources exist in the present sample, but its extent is not enough to lead to secure conclusions.

Acknowledgements. This work is based on observations made with the James Clerk Maxwell Telescope, operated by the Joint Astronomy Centre on behalf of the Science and Technology Facilities Council of the UK, and was supported in part by the European Community's Marie Curie Actions – Human Resource and Mobility within the JETSET (Jet Simulations, Experiments and Theory) network under contract MRTN-CT-2004 05592. The Centre for Star and Planet Formation is funded by the Danish National Research Foundation and the University of Copenhagen's programme of excellence.

References

Andre, P., Ward-Thompson, D., & Barsony, M. 1993, ApJ, 406, 122
Bachiller, R., Martin-Pintado, J., & Fuente, A. 1991, A&A, 243, L21
Bontemps, S., Andre, P., Terebey, S., & Cabrit, S. 1996, A&A, 311, 858
Cabrit, S., & Bertout, C. 1990, ApJ, 348, 530
Cabrit, S., & Bertout, C. 1992, A&A, 261, 274
Cambrésy, L. 1999, A&A, 345, 965
Casali, M. M., Eiroa, C., & Duncan, W. D. 1993, A&A, 275, 195
Choi, M., Evans, II, N. J., & Jaffe, D. T. 1993, ApJ, 417, 624
Curiel, S., Rodriguez, L. F., Moran, J. M., & Canto, J. 1993, ApJ, 415, 191
Davis, C. J., Matthews, H. E., Ray, T. P., Dent, W. R. F., & Richer, J. S. 1999, MNRAS, 309, 141
de Lara, E., Chavarria-K., C., & Lopez-Molina, G. 1991, A&A, 243, 139
Dent, W., Duncan, W., Ellis, M., et al. 2000, in Imaging at Radio through Submillimeter Wavelengths, ed. J. G. Mangum, & S. J. E. Radford, ASP Conf. Ser., 217, 33
Downes, T. P., & Cabrit, S. 2007, A&A, 471, 873
Eiroa, C., & Casali, M. M. 1992, A&A, 262, 468
Eiroa, C., Palacios, J., Eisloffel, J., Casali, M. M., & Curiel, S. 1997, in Herbig-Haro Flows and the Birth of Stars, ed. B. Reipurth, & C. Bertout, IAU Symp., 182, 103P
Eiroa, C., Torrelles, J. M., Curiel, S., & Djupvik, A. A. 2005, AJ, 130, 643
Enoch, M. L., Young, K. E., Glenn, J., et al. 2006, ApJ, 638, 293
Enoch, M. L., Glenn, J., Evans, II, N. J., et al. 2007, ApJ, 666, 982
Enoch, M. L., Evans, II, N. J., Sargent, A. I., & Glenn, J. 2009, ApJ, 692, 973
Evans, II, N. J., Allen, L. E., Blake, G. A., et al. 2003, PASP, 115, 965
Fuller, G. A., & Ladd, E. F. 2002, ApJ, 573, 699
Garay, G., Mardones, D., Rodríguez, L. F., Caselli, P., & Bourke, T. L. 2002, ApJ, 567, 980
Giovannetti, P., Caux, E., Nadeau, D., & Monin, J.-L. 1998, A&A, 330, 990
Gomez de Castro, A. I., Eiroa, C., & Lenzen, R. 1988, A&A, 201, 299
Graves, S. F., Richer, J. S., Buckle, J. V., et al. 2010, [arXiv:1006.0891]
Gregersen, E. M., Evans, II, N. J., Zhou, S., & Choi, M. 1997, ApJ, 484, 256
Haisch, Jr., K. E., Barsony, M., Greene, T. P., & Ressler, M. E. 2002, AJ, 124, 2841
Harvey, P., Merín, B., Huard, T. L., et al. 2007, ApJ, 663, 1149
Hatchell, J., & Dunham, M. M. 2009, A&A, 502, 139
Hatchell, J., Fuller, G. A., & Richer, J. S. 2007a, A&A, 472, 187
Hatchell, J., Fuller, G. A., Richer, J. S., Harries, T. J., & Ladd, E. F. 2007b, A&A, 468, 1009
Herbst, T. M., Beckwith, S. V. W., & Robberto, M. 1997, ApJ, 486, L59
Hodapp, K. W. 1999, AJ, 118, 1338
Hogerheijde, M. R., van Dishoeck, E. F., Salverda, J. M., & Blake, G. A. 1999, ApJ, 513, 350
Huard, T. L., Weintraub, D. A., & Kastner, J. H. 1997, MNRAS, 290, 598
Hurt, R. L., & Barsony, M. 1996, ApJ, 460, L45
Johnstone, D., Wilson, C. D., Moriarty-Schieven, G., et al. 2000, ApJ, 545, 327
Jørgensen, J. K., Harvey, P. M., Evans, II, N. J., et al. 2006, ApJ, 645, 1246
Kaas, A. A. 1999, AJ, 118, 558
Kaas, A. A., Olofsson, G., Bontemps, S., et al. 2004, A&A, 421, 623
Larsson, B., Liseau, R., Men'shchikov, A. B., et al. 2000, A&A, 363, 253
Lightfoot, J. F., Dent, W. R. F., Willis, A. G., & Hovey, G. J. 2000, in Astronomical Data Analysis Software and Systems IX, ed. N. Manset, C. Veillet, & D. Crabtree, ASP Conf. Ser., 216, 502
Mangum, J. G., Latter, W. B., & McMullin, J. P. 1996, in CO: Twenty-Five Years of Millimeter-Wave Spectroscopy, ed. W. B. Latter, J. E. Radford Simon, P. R. Jewell, J. G. Mangum, & J. Bally, IAU Symp., 170, 76P
Narayanan, G., Moriarty-Schieven, G., Walker, C. K., & Butner, H. M. 2002, ApJ, 565, 319
Padgett, D. L., Rebull, L. M., Stapelfeldt, K. R., et al. 2008, ApJ, 672, 1013
Rebull, L. M., Stapelfeldt, K. R., Evans, II, N. J., et al. 2007, ApJS, 171, 447
Reipurth, B., & Eiroa, C. 1992, A&A, 256, L1
Richer, J. S., Shepherd, D. S., Cabrit, S., Bachiller, R., & Churchwell, E. 2000, Protostars and Planets IV, 867
Rodriguez, L. F., Curiel, S., Moran, J. M., et al. 1989, ApJ, 346, L85
Smith, H., Buckle, J., Hills, R., et al. 2008, in SPIE Conf. Ser., 7020
Stanke, T., Smith, M. D., Gredel, R., & Khanzadyan, T. 2006, A&A, 447, 609
Strom, S. E., Vrba, F. J., & Strom, K. M. 1976, AJ, 81, 638
Sugitani, K., Nakamura, F., Tamura, M., et al. 2010, ApJ, 716, 299
Testi, L., & Sargent, A. I. 1998, ApJ, 508, L91
Testi, L., Sargent, A. I., Olmi, L., & Onello, J. S. 2000, ApJ, 540, L53
Torrelles, J. M., Gómez, J. F., Curiel, S., et al. 1992, ApJ, 384, L59
White, G. J., Casali, M. M., & Eiroa, C. 1995, A&A, 298, 594
Williams, J. P., & Myers, P. C. 2000, ApJ, 537, 891
Winston, E., Megeath, S. T., Wolk, S. J., et al. 2007, ApJ, 669, 493
Wolf-Chase, G. A., Barsony, M., Wootten, H. A., et al. 1998, ApJ, 501, L193
Wu, Y., Wei, Y., Zhao, M., et al. 2004, A&A, 426, 503
Ziener, R., & Eislöffel, J. 1999, A&A, 347, 565